

An integrated extended Kalman filter–implicit level set algorithm for monitoring planar hydraulic fractures

A Peirce and F Rochinha

Department of Mathematics, University of British Columbia, Vancouver, British Columbia,
V6T 1Z2, Canada
Mechanical Engineering Department, Federal University of Rio de Janeiro, Brazil

Received 12 May 2011, in final form 2 December 2011

Published 21 December 2011

Online at stacks.iop.org/IP/28/015009

Abstract

We describe a novel approach to the inversion of elasto-static tiltmeter measurements to monitor planar hydraulic fractures propagating within three-dimensional elastic media. The technique combines the extended Kalman filter (EKF), which predicts and updates state estimates using tiltmeter measurement time-series, with a novel implicit level set algorithm (ILSA), which solves the coupled elasto-hydrodynamic equations. The EKF and ILSA are integrated to produce an algorithm to locate the unknown fracture-free boundary. A scaling argument is used to derive a strategy to tune the algorithm parameters to enable measurement information to compensate for unmodeled dynamics. Synthetic tiltmeter data for three numerical experiments are generated by introducing significant changes to the fracture geometry by altering the confining geological stress field. Even though there is no confining stress field in the dynamic model used by the new EKF-ILSA scheme, it is able to use synthetic data to arrive at remarkably accurate predictions of the fracture widths and footprints. These experiments also explore the robustness of the algorithm to noise and to placement of tiltmeter arrays operating in the near-field and far-field regimes. In these experiments, the appropriate parameter choices and strategies to improve the robustness of the algorithm to significant measurement noise are explored.

(Some figures may appear in colour only in the online journal)

1. Introduction

Hydraulic fractures (HF) are a class of brittle fractures that propagate in pre-stressed solid media due to the injection of a viscous fluid. These fractures occur naturally when pressurized magma from deep underground chambers form vertical intrusions driven by buoyancy forces [34, 28]. HF have also found numerous industrial applications. In the oil and gas industry, HF are deliberately created in reservoirs to enhance the recovery of hydrocarbons by the creation of permeable pathways [5]. In the mining industry, HF have been used to enhance the block-caving process [12, 38] by weakening the rock surrounding underground excavations. HF have

also been used in producing geothermal energy, in waste disposal, protecting environmentally sensitive areas and may play a key role in CO₂ sequestration.

Recently, there has been considerable concern raised about hydraulic fractures propagating into subterranean water reservoirs leading to pollution of agricultural and domestic water supplies. There is thus interest in being able to monitor the progress of propagating HF. Unfortunately, other than the fluid pressure history at the well bore and the volume of fluid pumped, there is very little information readily available during the HF treatment process.

Tiltmeters have been used to monitor propagating HF since the late 1960s [36]. This technology has developed to the level that commercial HF monitoring services are routinely provided to the oil and gas industry [26]. Tiltmeters measure changes in the inclination of the rock at selected sample points due to the altered displacement gradient field induced by propagating HF. These tiltmeters can be located in the well bore itself, in neighboring off-set boreholes, or on the Earth's surface [6, 41, 16]. Interest in this form of monitoring has been mixed as the information that can be extracted from the inversion of the displacement gradient solution of the elliptic, elasto-static, PDE is limited due to the rapid $O(1/r^3)$ decay of this field with distance from the fracture. Indeed, this is a classic ill-posed inverse problem in which it is only feasible to invert the first two moments of the crack opening displacement from remote displacement gradient measurements [17]. This has likely hampered the development and deployment of extensive tiltmeter arrays in practice. In fact, the more recent development in the petroleum industry has been toward monitoring microseismic images [43], or a combination of tiltmeter and microseismic data [40]. While microseismic networks, based on the hyperbolic, elasto-dynamic PDE provide different information, it is difficult to distinguish the first motions due to the propagating HF from a secondary cloud of movements triggered in the jointed rockmass that surrounds the HF.

The approach to the tiltmeter inversion problem that we adopt in this paper is somewhat different. Following our initial study using the extended Kalman filter (EKF) for the inversion of tiltmeter data from a one-dimensional (1D) HF propagating in a state of plane strain [29], we consider the application of this methodology to monitoring two-dimensional planar HF. In 1D, the identification of the free boundary involves the location of only two points, while the determination of the crack opening involves the identification of a 1D function on the domain defined by these free boundary points. The planar problem is a lot more complex. Locating the free boundary involves identifying a closed curve in a plane, while identifying the crack opening involves determining a surface defined on the domain circumscribed by this unknown boundary curve. Rather than solving the isolated ill-posed tiltmeter inversion problems *at each time-step*, which is the approach traditionally used for this problem, we formulate a different inverse problem using the same data by stringing together the elasto-static tilt snapshots at each tiltmeter station into a time-series. These time-series of tilt measurements are then combined with a dynamic model for the fracture propagation to arrive at improved estimates of the fracture geometry and opening via the EKF. Instead of explicitly parameterizing the fracture-free boundary, which can be included into an augmented state vector for direct identification by the EKF, we choose to use the implicit level set algorithm (ILSA) to locate the free boundary by using local tip asymptotics along with EKF-generated state estimates comprising only the fracture width. It is this integrated EKF-ILSA scheme that we describe in this paper.

Traditional data assimilation methods rely on the Bayesian inference-based Kalman filter and its extensions [1, 15]. The EKF has been used extensively for inverse problems related to a wide range of applications (see for example [18, 31, 10, 21]) and in particular for fracture problems [2, 19]. In [2, 19], the EKF has been used to identify parameters from experiments in a cohesive crack model by considering a pseudo-time-stepping of the flow of experimental data and sequential estimation by the EKF. In contrast, we are using the EKF to compensate

for significant unmodeled dynamics in a complex system of highly nonlinear integro-partial differential equations. The objective of this inversion problem is not only to identify some parameters in the model, but also to identify large perturbations in both the crack opening displacement and the fracture geometry.

In section 2, we describe the forward hydraulic fracture model comprising a system of integro-partial differential equations along with a free-boundary problem and outline the novel ILSA numerical algorithm to locate the free boundary. In section 3, we provide a brief introduction to the EKF formulation that we use in this paper and present the details of the integrated EKF-ILSA scheme that we propose. In section 4, we provide the results of numerical experiments chosen to demonstrate the performance of the EKF-ILSA scheme for three distinct problems in which significant geometric perturbations are introduced by changes in the confining geological stress field; in section 5 we provide some concluding remarks.

2. Forward model for a planar hydraulic fracture

2.1. Governing equations

Hydraulic fractures tend to propagate in planar regions perpendicular to the minimum principal direction of the geological confining stress field. The dynamics of the propagating HF are governed by a coupled system of nonlinear, degenerate, hyper-singular, integro-partial differential equations along with propagation and boundary conditions that determine the location of the fracture-free boundary. The numerical solution of these equations presents considerable challenges, including: (i) the resolution of the multiscale, singular solution structure close to the fracture tip; (ii) due to this singular tip behavior the front velocity involves an indeterminate form expression that is difficult to evaluate numerically and as a result the free boundary cannot be located using standard moving boundary algorithms; (iii) a spatial discretization reduces the problem to a stiff system of ODEs for which implicit backward difference time-stepping and specialized algorithms for the solution of the coupled equations at each time-step are necessary [23].

Recently, the ILSA scheme [24] has been developed for the efficient solution of this complex-free boundary problem. This scheme is able to incorporate multiscale tip behavior, obtained via detailed asymptotic analysis [7, 8, 20], into an algorithm defined on a relatively coarse structured Eulerian mesh. This ILSA solution scheme forms the basis for the forward model that is used in this paper in combination with the EKF to devise a novel HF monitoring technique. Since all the numerical experiments presented are in dimensionless form, for the sake of brevity, we choose to only present the dimensionless form of the model equations and details of their discretization. The dimensional equations and their reduction to the dimensionless form are detailed in [24]. We also consider the host rock in which the HF is growing to comprise an impermeable elastic medium.

We consider a coordinate system (χ, η, ζ) and a dimensionless timescale τ . The evolving fracture is assumed to occupy the region $\mathcal{S}(\tau)$ in the (χ, η) -plane that is circumscribed by the fracture front $\partial\mathcal{S}(\tau)$ (see figure 1). The dimensionless quantities \mathcal{G}_j that appear in the equations below are defined to be

$$\mathcal{G}_e = \frac{E'W_*}{P_*L_*}, \quad \mathcal{G}_m = \frac{\mu' L_*^2}{W_*^2 P_* T_*}, \quad \mathcal{G}_v = \frac{Q_0 T_*}{W_* L_*^2}, \quad \mathcal{G}_k = \frac{K' L_*^{1/2}}{E' W_*}. \quad (2.1)$$

Here, $E' = \frac{E}{1-\nu^2}$, where E and ν are the rock Young's modulus and Poisson's ratio; $\mu' = 12\mu$, where μ is the dynamic fluid viscosity, and $K' = 4\left(\frac{2}{\pi}\right)^{\frac{1}{2}} K_{IC}$ is the modified stress intensity factor. In addition, T_* is a characteristic timescale, W_* is a characteristic fracture aperture, P_*

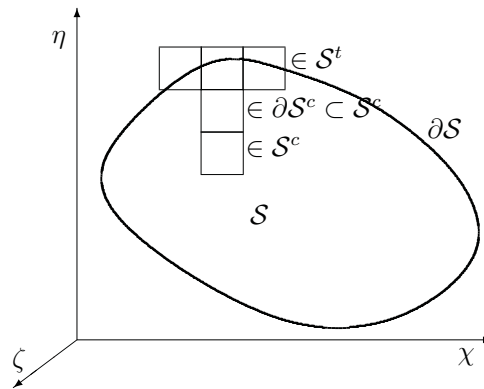


Figure 1. A schematic of a hydraulic fracture occupying the region \mathcal{S} in the χ – η plane. The squares represent the structured mesh used by the ILSA scheme to discretize the governing equations. The sets \mathcal{S}^t , \mathcal{S}^c and $\partial\mathcal{S}^c$ are used to identify different classes of elements that are used in the ILSA scheme described in subsection 2.3.

is a characteristic net pressure, L_* is a characteristic length scale and Q_0 is the characteristic volumetric fluid injection rate.

2.1.1. The elasticity equation. The hypersingular integral equation [9] relating the crack opening displacement $\Omega(\chi, \eta, \tau)$ to the fluid pressure $\Pi_f(\chi, \eta, \tau)$ is given by

$$\Pi = \Pi_f(\chi, \eta, \tau) - \Sigma_o \varphi(\chi, \eta) = -\frac{\mathcal{G}_e}{8\pi} \int_{\mathcal{S}(\tau)} \frac{\Omega(\chi', \eta', \tau) d\mathcal{S}(\chi', \eta')}{[(\chi' - \chi)^2 + (\eta' - \eta)^2]^{3/2}}. \quad (2.2)$$

Here, $\Sigma_o = \frac{\sigma_o}{P_*}$ is the dimensionless confining stress where σ_o is the characteristic confining stress, $\varphi(\chi, \eta)$ represents the spatial variation of the confining stress field and $\Pi = \Pi_f - \Sigma_o \varphi(\chi, \eta)$ is the net pressure.

2.1.2. The fluid flow equation. A combination of Poiseuille's law and the conservation of mass with a point source $\mathcal{G}_v \psi(\tau) \delta(\chi, \eta)$ yields Reynolds' lubrication equation, which assumes the form

$$\frac{\partial \Omega}{\partial \tau} = \frac{1}{\mathcal{G}_m} \nabla \cdot (\Omega^3 \nabla \Pi_f) + \mathcal{G}_v \psi(\tau) \delta(\chi, \eta). \quad (2.3)$$

2.1.3. Boundary and propagation conditions. A zero flux boundary condition and an LEFM asymptotic propagation condition [27], which require that the local stress intensity factor be in limit equilibrium with the dimensionless toughness \mathcal{G}_k , respectively, assume the form

$$\lim_{\xi \rightarrow 0} \Omega^3 \frac{\partial \Pi_f}{\partial \xi} = 0 \quad \text{and} \quad \lim_{\xi \rightarrow 0} \frac{\Omega}{\xi^{1/2}} = \mathcal{G}_k, \quad (2.4)$$

where ξ is a local coordinate representing the normal distance to the free-boundary $\partial\mathcal{S}(\tau)$.

2.1.4. Propagation regimes and multiscale tip behavior. If $\mathcal{G}_k > 0$, then the asymptotic behavior of the fracture opening is always given by the second equation in (2.4). However, this classic LEFM square root behavior may not be the appropriate asymptotic expansion that applies at the computational length scale. There are, in the absence of a fluid lag, two

competing dissipative processes, namely the viscous dissipation, associated with driving the fluid into the fracture cavity, and the energy required to fracture the rock, which is associated with the fracture toughness [24]. Since the objective of this paper is to explore the performance of a combined EKF-ILSA algorithm rather than this multiscale behavior, we choose to restrict the examples presented in this study to solutions in the neighborhood of the viscous solution for which $\mathcal{G}_k = 0$. This regime of propagation has been shown to be ubiquitous for practical HF treatments [30]. Physically, this solution corresponds to an HF propagating between two de-bonded impermeable half-spaces. For the plane strain case [4, 7, 8, 20] and for arbitrarily shaped planar fractures with smooth boundaries [24], the tip asymptotic behavior of the fracture opening Ω for an HF propagating with a velocity $v = \lim_{\xi \rightarrow 0} \Omega^2 \frac{\partial \Pi_l}{\partial \xi}$ has been shown to be of the form

$$\Omega \stackrel{\xi \rightarrow 0}{\sim} \beta_{m0} v^{1/3} \xi^{2/3}, \quad \beta_{m0} = 2^{1/3} \cdot 3^{5/6}. \quad (2.5)$$

This asymptotic behavior (2.5) plays a central role in locating the free-boundary $\partial \mathcal{S}(\tau)$ in the ILSA scheme.

2.2. Discrete equations

We assume [24] that the fracture will grow within a rectangular region that has been tessellated into a fixed uniform rectangular mesh with spacings $\Delta \chi$ and $\Delta \eta$ in the two coordinate directions. The fracture footprint $\mathcal{S}(\tau)$ is then covered by rectangular elements $\Delta \mathcal{S}_{m,n}$ such that $\mathcal{S} \subseteq \cup \Delta \mathcal{S}_{m,n}$. Constant displacement discontinuity (DD) elements are used for the elasticity computations [3] along with collocation at element centers, while the lubrication equation is discretized by replacing spatial derivatives by second-order finite difference quotients to yield a five-node finite difference stencil [35]. The resulting, extremely stiff, system of ODEs is solved using the backward Euler scheme.

2.2.1. The discrete elasticity equation. The elasticity equation (2.2) is discretized by assuming that the fracture opening $\Omega(\chi, \eta, \tau)$ is piecewise constant over each rectangular element $\Delta \mathcal{S}_{m,n}$, i.e.

$$\Omega(\chi, \eta, \tau) = \sum_{m,n} \Omega_{mn}(\tau) H_{mn}(\chi, \eta), \quad \text{where} \quad H_{mn}(\chi, \eta) = \begin{cases} 1 & \text{for } (\chi, \eta) \in \Delta \mathcal{S}_{m,n} \\ 0 & \text{for } (\chi, \eta) \notin \Delta \mathcal{S}_{m,n} \end{cases} \quad (2.6)$$

and $H_{mn}(\chi, \eta)$ is the characteristic function for element (m, n) . Substituting (2.6) into (2.2) and evaluating the pressures at the element-centered collocation points yield a system of algebraic equations of the form

$$\Pi_{kl}(\tau) = \sum_{m,n} C_{k-m, l-n} \Omega_{mn}(\tau), \quad (2.7)$$

where

$$C_{k-m, l-n} = -\frac{1}{8\pi} \left[\frac{\sqrt{(\chi_k - \chi)^2 + (\eta_l - \eta)^2}}{(\chi_k - \chi)(\eta_l - \eta)} \right]_{\chi=\chi_m+\Delta\chi, \eta=\eta_n+\Delta\eta}^{\chi=\chi_m-\Delta\chi, \eta=\eta_n-\Delta\eta}.$$

It is convenient to write (2.7) in the operator form

$$\Pi = C\Omega. \quad (2.8)$$

2.2.2. *The discrete fluid flow equation.* In order to discretize the fluid flow equation (2.3) in a way that is compatible with (2.7), we use the pressures $\Pi_{kl}(\tau)$ and widths $\Omega_{kl}(\tau)$ at element centers along with central difference approximations of the partial derivatives to arrive at the following spatial discretization:

$$\begin{aligned} \frac{d}{d\tau}\Omega_{kl}(\tau) = & \frac{1}{\Delta\chi} \left(\Omega_{k+\frac{1}{2}l}^3 \frac{(\Pi_{k+1l} - \Pi_{kl})}{\Delta\chi} - \Omega_{k-\frac{1}{2}l}^3 \frac{(\Pi_{kl} - \Pi_{k-1l})}{\Delta\chi} \right) \\ & + \frac{1}{\Delta\eta} \left(\Omega_{kl+\frac{1}{2}}^3 \frac{(\Pi_{kl+1} - \Pi_{kl})}{\Delta\eta} - \Omega_{kl-\frac{1}{2}}^3 \frac{(\Pi_{kl} - \Pi_{kl-1})}{\Delta\eta} \right) + s_{kl}(\tau), \end{aligned} \quad (2.9)$$

where $s_{kl}(\tau)$ represents the source and sink terms that apply to the element located at (χ_k, η_l) and $\Omega_{k+\frac{1}{2}l}$, etc, represent the aperture values at element edges that are determined by the following averaging operator $\Omega_{k+\frac{1}{2}l} = \frac{1}{2}(\Omega_{k+1l} + \Omega_{kl})$. It is convenient to express this system of differential equations in the following operator form:

$$\frac{d\Omega}{d\tau} = A(\Omega)\Pi + s(\tau), \quad (2.10)$$

where $A(\Omega)$ is the second-order difference operator defined on the right-hand side of (2.9).

2.2.3. *Coupled evolution operator: backward Euler scheme.* Using (2.8) to eliminate the pressure Π from (2.10), we obtain the following evolution equation for Ω :

$$\frac{d\Omega}{d\tau} = A(\Omega)C\Omega + s(\tau), \quad (2.11)$$

where $s(\tau)$ represents the source vector. The evolution operator $A(\Omega)C$ can be shown [25] to be extremely stiff resulting in a CFL condition of the form $\Delta\tau \leq O(\min\{\Delta\chi^3, \Delta\eta^3\})$ for explicit time-stepping. We therefore use the L-stable backward Euler scheme to march the solution process forward in time, resulting in the following system of nonlinear equations for $\Omega(\tau + \Delta\tau)$ that need to be solved at each time-step:

$$\Omega(\tau + \Delta\tau) - \Omega(\tau) = \Delta\tau A(\Omega(\tau + \Delta\tau))C\Omega(\tau + \Delta\tau) + \Delta\tau s(\tau + \Delta\tau). \quad (2.12)$$

Introducing the notation $\Delta\Omega := \Omega(\tau + \Delta\tau) - \Omega(\tau)$ we may express (2.12) in the following form suitable for fixed point iteration to determine $\Omega(\tau + \Delta\tau) = \lim_{i \rightarrow \infty} \Omega^i$:

$$\begin{aligned} (I - \Delta\tau A(\Omega^i)C)\Delta\Omega^i &= \Delta\tau A(\Omega^i)C\Omega(\tau) + \Delta\tau s(\tau + \Delta\tau) \\ \Omega^{i+1} &= \Omega(\tau) + \Delta\Omega^i. \end{aligned} \quad (2.13)$$

2.3. The implicit level set algorithm (ILSA)

The fundamental *ansatz* behind the ILSA scheme is that a given tip asymptote applies at the computational length scale, which is characterized by the mesh size $O(\Delta\chi, \Delta\eta)$. In this paper, we assume that the viscous tip asymptote (2.5) holds one or two cell lengths from the tip. In order to locate the free boundary, we assume that an initial estimate of the fracture footprint is known and solve the coupled equations (2.12) for $\Omega(\tau + \Delta\tau)$. The apertures nearest to the tip are then used to obtain a new estimate for the normal distance to the fracture tip by inverting (2.5). To implement this iterative procedure, we divide the elements $\{\Delta\mathcal{S}_{m,n}\}$ that cover the region \mathcal{S} occupied by the fracture in the current iteration into two disjoint sets, \mathcal{S}^c and \mathcal{S}^f . The elements totally within the boundary $\partial\mathcal{S}$ are referred to as the ‘channel elements’ and occupy the region \mathcal{S}^c . Those partially filled elements that intersect the crack front are called ‘tip elements’, which occupy the region \mathcal{S}^f (see figure 1). Thus, $\mathcal{S}^c \subset \mathcal{S}$, $\partial\mathcal{S} \cap \mathcal{S}^c = \emptyset$ and $\mathcal{S} \subset \mathcal{S}^c \cup \mathcal{S}^f = \cup \Delta\mathcal{S}_{m,n}$. As our reference points that we use to estimate the normal distance

to the free boundary, we choose the ribbon of elements $\partial\mathcal{S}^c \subset \mathcal{S}^c$, each of which share at least one side with a tip element in \mathcal{S}^f . The current trial solution for Ω at the centers of the ribbon elements $\partial\mathcal{S}^c$ combined with the asymptotic relation (2.5) provide the boundary conditions for the eikonal equation

$$|\nabla\mathcal{T}(\chi, \eta)| = 1. \quad (2.14)$$

The solution of (2.14) is the signed distance function whose level set $\mathcal{T}(\chi, \eta) = 0$ is the fracture front $\partial\mathcal{S}$.

We adopt the convention that $\mathcal{T} < 0$ for points inside the fracture boundary and $\mathcal{T} > 0$ outside the fracture boundary. Then, assuming that the fracture is evolving under a viscous mode of propagation, we invert (2.5) to obtain

$$\mathcal{T}(\chi, \eta) = -\xi \sim -\left(\frac{\Omega}{\beta_{m0} v^{1/3}}\right)^{3/2} \quad \text{for all } (\chi, \eta) \in \partial\mathcal{S}^c. \quad (2.15)$$

Rather than using the indeterminate form expression for the front velocity $v = \lim_{\xi \rightarrow 0} \Omega^2 \frac{\partial \Pi_f}{\partial \xi}$, which is difficult to evaluate numerically with any precision, we use the following expression for the front velocity in terms of two successive signed distance functions

$$v = -\frac{\mathcal{T}_{\tau+\Delta\tau} - \mathcal{T}_\tau}{\Delta\tau}. \quad (2.16)$$

Eliminating v from (2.15) using (2.16) reduces the problem of determining $\mathcal{T}(\chi, \eta, \tau + \Delta\tau)$ for $(\chi, \eta) \in \partial\mathcal{S}^c$ to that of solving the cubic equation:

$$\mathcal{T}_{\tau+\Delta\tau}^3 - \mathcal{T}_\tau \mathcal{T}_{\tau+\Delta\tau}^2 + \Delta\tau \left(\frac{\Omega_{\tau+\Delta\tau}}{\beta_{m0}}\right)^3 = 0. \quad (2.17)$$

Since $\mathcal{T}_\tau < 0$, an application of Descarte's rule implies that (2.17) has only one negative real root, which determines the boundary condition values $\mathcal{T}(\chi, \eta, \tau + \Delta\tau)$ for $(\chi, \eta) \in \partial\mathcal{S}^c$ uniquely. Having determined the boundary values for \mathcal{T} , an upwind differencing scheme, developed for the numerical solution of conservation laws [22, 33], is used to solve (2.14) for $\mathcal{T}(\chi, \eta, \tau + \Delta\tau)$ in the immediate neighborhood of the crack front using the fast marching method (FMM) (for further details see [22, 33, 24]). The fracture front is then determined by locating the curve $\mathcal{T}(\chi, \eta, \tau + \Delta\tau) = 0$.

2.4. Tiltmeter observation model

For the observation model to be used in conjunction with the EKF in this paper, we consider the time-series of displacement gradients due to the evolving fracture surface measured by a distant array of tiltmeters. Tiltmeters measure the angles between their axes and the gravity vector, which are related to the curl of the local displacement field [16], i.e. $\omega = \nabla \times \mathbf{u}$, where $\mathbf{u} = (u_1, u_2, u_3) = (u_\chi, u_\eta, u_\zeta)$ is the local displacement vector at each of the tilts.

In order to relate these displacement gradients to the evolving hydraulic fracture, we make use of the following expression for the displacement field due to a planar crack occupying the region $\mathcal{S}(\tau)$ in the χ - η plane. For a crack having an opening displacement Ω in the ζ -direction normal to the fracture plane, the scaled displacement components u_k are given by

$$u_k(\chi, \eta, \zeta, \tau) = \frac{1}{8\pi(1-\nu)} \int_{\mathcal{S}(\tau)} \Omega(\chi', \eta', \tau) \mathcal{U}_k(\chi - \chi', \eta - \eta', \zeta) d\mathcal{S}(\chi', \eta'), \quad (2.18)$$

where $\mathcal{U}_k(\chi, \eta, \zeta)$ can be expressed [32, 3] in terms of derivatives of the harmonic function $\Phi(\chi, \eta, \zeta) = \frac{1}{\rho}$, where $\rho = \sqrt{\chi^2 + \eta^2 + \zeta^2}$, as follows:

$$\mathcal{U}_\chi = -(1-2\nu)\Phi_{,\chi} - \zeta\Phi_{,\chi\zeta}; \quad \mathcal{U}_\eta = -(1-2\nu)\Phi_{,\eta} - \zeta\Phi_{,\eta\zeta}; \quad \mathcal{U}_\zeta = 2(1-\nu)\Phi_{,\zeta} - \zeta\Phi_{,\zeta\zeta}. \quad (2.19)$$

For rectangular elements, such as the $\Delta S_{m,n}$ used to discretize the fracture plane \mathcal{S} , it is convenient to determine the integral of Φ , which we represent by $\bar{\Phi}$, over a typical rectangle and to evaluate the following fundamental derivatives: $\bar{\Phi}_{,\chi} = \log(\rho + (\eta - \eta'))$, $\bar{\Phi}_{,\eta} = \log(\rho + (\chi - \chi'))$ and $\bar{\Phi}_{,\xi} = \arctan\left(\frac{\rho\xi}{(\eta - \eta')(\chi - \chi')}\right)$, where the limits of integration $\int_{\chi' = -\frac{\Delta\chi}{2}}^{\chi' = \frac{\Delta\chi}{2}} \int_{\eta' = -\frac{\Delta\eta}{2}}^{\eta' = \frac{\Delta\eta}{2}}$ have been omitted. The remaining higher order derivatives required to produce the rotation vector ω can be obtained from these expressions for $\bar{\Phi}_{,k}$ by direct differentiation.

3. The integrated EKF-ILSA

In this section, we describe the integrated EKF-ILSA scheme for monitoring evolving hydraulic fractures. A particularly challenging aspect of this problem is capturing the moving fracture boundary. Rather than parameterizing the free boundary and defining an augmented set of state variables to locate the free boundary explicitly using the EKF, we choose to use the ILSA scheme to locate the fracture-free boundary using tip widths that have been corrected by the EKF to account for tiltmeter measurements.

3.1. The extended Kalman filter (EKF)

The Kalman filter [1] provides the optimal linear estimator for the underlying state of a linear dynamical system, at a given time, which takes into account all the observations up till that time. The EKF [1, 15] applies this Kalman filter methodology to nonlinear dynamical systems by linearizing the system about a nominal state comprising the current state estimate. Naturally, as with all such linearizations, its validity depends on how close the current estimate is to the actual state (see [1]).

We summarize the EKF formulation [1, 15] that we use in the EKF-ILSA scheme. We consider a typical time interval $[\tau_k, \tau_{k+1}]$ and re-write the discrete dynamical system and observer models defined in section 2 as follows:

$$x_{k+1} = f_k(x_k) + w_k \quad (3.1)$$

$$y_k = H_k x_k + v_k, \quad (3.2)$$

where the state vector x_k contains the discrete widths $\{\Omega_{mn}(\tau_k)\}$ and the observation vector y_k contains the rotation components $\{\omega_i(\tau_k)\}$ observed at the tiltmeter stations at time τ_k , and $w_k \sim N(0, \Gamma_{w_k})$ and $v_k \sim N(0, \Gamma_{v_k})$ are assumed to be independent, normally distributed, random variables with covariance matrices Γ_{w_k} and Γ_{v_k} , respectively. The matrix Γ_{w_k} represents unmodeled dynamics while Γ_{v_k} represents noise in the measurements themselves or uncertainty in the measurement model. Here $f_k(\cdot)$ is defined implicitly by the operator equation

$$(I - \Delta\tau A(\Omega(\tau_{k+1}))C)\Omega(\tau_{k+1}) = \Omega(\tau_k) + \Delta\tau s(\tau_{k+1}) \quad (3.3)$$

and H_k is the discretized operator defined in (2.18) that maps the fracture widths x_k to the tiltmeter rotations y_k .

We define $\hat{x}_{k|j} := E[x_k | x_{1:j}, y_{1:j}]$ to be the state estimate at time τ_k given all the data up to time τ_j . Similarly, we define $\Gamma_{k|j} := E[(x - \hat{x}_{k|j})(x - \hat{x}_{k|j})^T | x_{1:j}, y_{1:j}]$ to be the state covariance matrix at time τ_k given all the data up to the time τ_j . The Jacobian for the coupled system $F_k = \frac{\partial f_k(\hat{x}_{k|k})}{\partial x}$ has the form

$$F_k = [I - \Delta\tau A(\Omega_{k|k})C - \Delta\tau A'(\Omega_{k|k})C\Omega_{k|k}]^{-1}, \quad (3.4)$$

where A' represents the derivative of A . We have found that by neglecting the term involving A' , we obtain the following fixed point operator (see (2.13)) approximation $F_k \approx [I - \Delta \tau A(\Omega_{k|k})C]^{-1}$, which proves to be more stable and computationally more efficient than that given in (3.4). The EKF can now be expressed in the following predictor-corrector form.

Prediction step

Given $\hat{x}_{k|k}$ and $\Gamma_{k|k}$ compute

$$\hat{x}_{k+1|k} = f_k(\hat{x}_{k|k}) \quad (3.5)$$

$$\Gamma_{k+1|k} = F_k \Gamma_{k|k} F_k^T + \Gamma_{w_k}. \quad (3.6)$$

Corrector step

Given the predicted values $\hat{x}_{k+1|k}$ and $\Gamma_{k+1|k}$ compute

$$K_{k+1} = \Gamma_{k+1|k} H_{k+1}^T (H_{k+1} \Gamma_{k+1|k} H_{k+1}^T + \Gamma_{v_{k+1}})^{-1} \quad (3.7)$$

$$\hat{x}_{k+1|k+1} = \hat{x}_{k+1|k} + K_{k+1} (y_{k+1} - h_{k+1}(\hat{x}_{k+1|k})) \quad (3.8)$$

$$\Gamma_{k+1|k+1} = (I - K_{k+1} H_{k+1}) \Gamma_{k+1|k}, \quad (3.9)$$

where the matrix K_{k+1} is the so-called Kalman gain. The initial estimate for the state is assumed to be the radial solution [30], i.e. $\hat{x}_{1|1} = \Omega(\tau_1)$. For the model and noise covariances, we assume that $\Gamma_{w_k} = \sigma_w^2 I$ and $\Gamma_{v_k} = \sigma_v^2 I$, and for an initial guess for the state covariance matrix we assume $\Gamma_{1|1} = \sigma_w^2 I$.

The scaled EKF equations and parameter choices

Because we will be typically dealing with remote measurements, which are typically small due to the rapid $O(\frac{1}{\rho^3})$ decay of the displacement gradient fields, it is useful to re-scale the update equations in order to gain insight into how the algorithm parameters should be selected. Since the measurements and the values of Green's function operator are going to be small, we introduce the following scaled variables:

$$\varepsilon = \|H_1\|_2, \quad H_k = \varepsilon \mathcal{H}_k, \quad y_k = \varepsilon \mathcal{Y}_k, \quad \text{and} \quad \Gamma_{ij} = \sigma_w^2 \mathcal{G}_{ij}.$$

The covariance prediction equation (3.6) assumes the form

$$\begin{aligned} \Gamma_{k+1|k} &= \sigma_w^2 \mathcal{G}_{k+1|k} \\ &= \sigma_w^2 (F_k \mathcal{G}_{k|k} F_k^T + I), \end{aligned}$$

while the expression for the Kalman Gain (3.8) can be rewritten in the form

$$\begin{aligned} K_{k+1} &= \varepsilon^{-1} \mathcal{G}_{k+1|k} \mathcal{H}_{k+1}^T (\mathcal{H}_{k+1} \mathcal{G}_{k+1|k} \mathcal{H}_{k+1}^T + \gamma I)^{-1} \\ &= \varepsilon^{-1} \mathcal{K}_{k+1}, \end{aligned}$$

where

$$\mathcal{K}_{k+1} := \mathcal{G}_{k+1|k} \mathcal{H}_{k+1}^T (\mathcal{H}_{k+1} \mathcal{G}_{k+1|k} \mathcal{H}_{k+1}^T + \gamma I)^{-1}$$

and

$$\gamma := \frac{\sigma_v^2}{\sigma_w^2 \varepsilon^2}. \quad (3.10)$$

Finally, in terms of these new scaled variables, the state correction can be expressed as follows:

$$\widehat{x}_{k+1|k+1} = \widehat{x}_{k+1|k} + \mathcal{K}_{k+1}(\mathcal{Y}_{k+1} - \mathcal{H}_{k+1}\widehat{x}_{k+1|k}).$$

The point of introducing this re-scaling is that the parameter γ defined in (3.10) provides insight into the choice of parameters σ_v and σ_w . If $\gamma \rightarrow 0$, then we observe that $\mathcal{K}_{k+1} \rightarrow \mathcal{H}_{k+1}^{-1}$, which implies that $\widehat{x}_{k+1|k+1} \rightarrow H_{k+1}^{-1}y_{k+1}$. In this limit, the Kalman filter places more emphasis on the measurements than on the dynamics of the model itself in arriving at an estimate of the state. This would be appropriate, for example, if there was significant uncertainty in the model, in which case σ_w would need to be large relative to σ_v . Alternatively, this situation might occur if the data were known to be significantly more accurate than the level of confidence in the model dynamics. Conversely, if $\sigma_w \rightarrow 0$, which would be the case if there was a great deal more confidence in the model dynamics than in the measurement process, then $\gamma \rightarrow \infty$ so that $\mathcal{K}_{k+1} \rightarrow 0$ and the change made by the Kalman filter to the state predicted by the model dynamics is negligible. In the experiments explored in this paper, we are interested in exploring situations in which there is significant unmodeled dynamics. Thus we would like to be operating in the regime in which $\gamma \ll 1$. A choice that we have found particularly effective is $\sigma_v = \phi\sigma_w\varepsilon$, which implies that $\gamma = \phi^2$. Here, ϕ is a parameter that can be used to adjust the resolution of the monitoring process. Values of ϕ are typically chosen in the range $0.01 < \phi < 2$ and can be used to adjust the weight that the EKF-ILSA scheme places on the measured data relative to the desired weight on the accuracy of the dynamics of the forward model.

3.2. The integrated algorithm

The integrated EKF-ILSA algorithm comprises the following two steps: (1) the discrete fracture widths Ω_{mn} are treated as the primary state variables that are updated using the EKF based on the coupled equations and observed data *while the fracture footprint is frozen*; (2) the fracture front positions are updated using the ILSA algorithm and the new estimates of the widths. Step (1), involving the EKF width prediction, and step (2), involving ILSA front correction, are then repeated until the front iterations converge. By this stage, both the widths and front positions are consistent with the dynamics of the forward models (2.2)–(2.5) and the observed data (2.18).

To distinguish between time-steps and front iterations, we use subscripts to denote time-step information and superscripts to denote the front iteration counter. Thus $\widehat{x}_{k+1|k}^j$ represents the predicted value for the state at time-step $k+1$ given all the data up till time-step k in the j th front iteration. If the superscript is absent, we assume that we are referring to the value of that quantity once all the front iterations have converged. In the convergence check below $\Xi(\mathcal{S})$ represents the characteristic function of \mathcal{S} . It is possible for the Kalman update to predict width components that are negative, i.e. $\widehat{x}_{k+1|k+1,i}^{j+1} < 0$, where the additional subscript refers to a particular component. These negative widths are likely to occur if the EKF-ILSA footprint has, in some region, gone beyond that of the synthetic fracture. We prevent this physically impossible situation by resetting those width components to the values predicted by the forward model, i.e. $\widehat{x}_{k+1|k+1,i}^{j+1} = \widehat{x}_{k+1|k,i}^j$. This strategy involves minimal adaptation of the standard ILSA scheme, while other schemes, which will add more robustness to the algorithm, such as the deletion of negative width elements from the active set or the imposition of a minimal width constraint are left to future investigations.

Initialization:

- Set the state to the radial exact solution $\widehat{x}_{|1} = \Omega_{\text{exact}}(\tau_1)$.
- Set the domain to the exact circle $\mathcal{S}_1 = \{(\chi, \eta) : \sqrt{(\chi - \chi_c)^2 + (\eta - \eta_c)^2} \leq \rho_{\text{exact}}(\tau_1)\}$.
- Set the EKF parameters ϕ , σ_w and the covariance matrix $\Gamma_{|1} = \sigma_w^2 I$.

Time-step loop: $k = 1 : N_t$

$$\tau_{k+1} = \tau_k + \Delta\tau.$$

Initialize guesses: set the front $\partial\mathcal{S}_{k+1}^1 = \partial\mathcal{S}_k$ and the covariance matrix $\Gamma_{k|k}^1 = \Gamma_{k|k}$.

Front iteration loop: $j = 1 : N_f$

Given $\hat{x}_{k|k}$ and $\partial\mathcal{S}_{k+1}^j$ solve (2.13) for $\hat{x}_{k+1|k}^j = f_k(\hat{x}_{k|k})$

Evaluate $F_k^j \approx [I - \Delta\tau A(\hat{x}_{k+1|k}^j)C]^{-1}$ and H_{k+1}^j

If $k=1$, set $\varepsilon = \|H_2^1\|_2 := \|H_1\|_2$ and then set $\sigma_v = \phi\sigma_w\varepsilon$

$$\Gamma_{k+1|k}^j = F_k^j \Gamma_{k|k}^j (F_k^j)^T + \Gamma_{w_k}$$

$$K_{k+1}^j = \Gamma_{k+1|k}^j (H_{k+1}^j)^T [H_{k+1}^j \Gamma_{k+1|k}^j (H_{k+1}^j)^T + \Gamma_{v_{k+1}}]^{-1}$$

$$\hat{x}_{k+1|k+1}^{j+1} = \hat{x}_{k+1|k}^j + K_{k+1}^j (y_{k+1} - H_{k+1}^j \hat{x}_{k+1|k}^j)$$

If $\hat{x}_{k+1|k+1}^{j+1, i} < 0$ set $\hat{x}_{k+1|k+1}^{j+1, i} = \hat{x}_{k+1|k}^j$ (to prevent negative widths).

$$\Gamma_{k+1|k+1}^{j+1} = (I - K_{k+1}^j H_{k+1}^j) \Gamma_{k+1|k}^j$$

Use $\hat{x}_{k+1|k+1}^{j+1}$ to set BC for \mathcal{T}_{k+1}^{j+1} along $\partial\mathcal{S}_{k+1}^{c,j}$ using (2.17) and use FMM to solve

$$|\nabla \mathcal{T}_{k+1}^{j+1}(\chi, \eta)| = 1.$$

Update the front position $\partial\mathcal{S}_{k+1}^{j+1} = \{(\chi, \eta) : \mathcal{T}_{k+1}^{j+1}(\chi, \eta) = 0\}$ and the velocity v_{k+1}^{j+1} field using (2.16).

Check for convergence $\|\Xi(\mathcal{S}_{k+1}^{j+1}) - \Xi(\mathcal{S}_{k+1}^j)\| < tol \times \Xi(\mathcal{S}_{k+1}^{j+1})$.

end front iteration loop

end time-step loop

4. Numerical results

4.1. Description of the numerical experiments

4.1.1. Geometric changes due to variations in the confining stress field. We now present results for a sequence of numerical experiments in which synthetic data at an array of tiltmeters has been created for hydraulic fractures propagating in situations in which significant changes to the geometry of the evolving fractures are induced by spatial variations in the confining stress field $\Sigma_o\varphi(\chi, \eta)$. Gaussian white noise with mean zero of varying amplitude σ_N between 0% and 5% is added to the tiltmeter data to simulate typical measurement errors experienced in the field. In the identification of the state and the fracture boundary by the EKF-ILSA scheme, the forward model used by the EKF assumes no confining stress field, i.e. $\varphi(\chi, \eta) = 0$. Thus without the corrections introduced by the EKF component of the algorithm due to the measured tiltmeter data, the solution produced by the dynamic model would correspond to a radially symmetric crack. This amounts to significant unmodeled dynamics that has to be compensated for by the EKF-ILSA algorithm.

4.1.2. Error measures. In order to be able to present the data in a compact form for ready comparison of the performance of the algorithm with different choices of the parameter ϕ , we introduce the following error measures:

$$\begin{aligned} \mathcal{E}_w(\tau_k; \phi, \sigma_N) &:= \frac{\int_{\mathcal{S}_k^s \cup \mathcal{S}_k^{E-I}} |\Omega^s(\chi, \eta, \tau_k) - \Omega^{E-I}(\chi, \eta, \tau_k)| d\mathcal{S}}{\int_{\mathcal{S}_k^s} |\Omega^s(\chi, \eta, \tau_k)| d\mathcal{S}}, \\ \mathcal{E}_F(\tau_k; \phi, \sigma_N) &:= \frac{\mathcal{A}[(\mathcal{S}_k^s \cup \mathcal{S}_k^{E-I}) \setminus (\mathcal{S}_k^s \cap \mathcal{S}_k^{E-I})]}{\mathcal{A}[\mathcal{S}_k^s]} \end{aligned} \quad (4.1)$$

where the operator $\mathcal{A}[\cdot]$ represents the area of the indicated region, \mathcal{S}_k^s is the region occupied by the synthetic fracture at time τ_k and \mathcal{S}_k^{E-I} represents the corresponding region occupied by the fracture identified by the EKF-ILSA scheme. $\mathcal{E}_w(\tau_k)$ represents the *relative width error* measured by the integral of absolute value of the difference between the widths over the combined region $\mathcal{S}_k^s \cup \mathcal{S}_k^{E-I}$ over which the two fractures fall divided by the total volume in the synthetic fracture. We assume that $\Omega^s = 0$ on $\mathcal{S}_k^{E-I} \setminus (\mathcal{S}_k^s \cap \mathcal{S}_k^{E-I})$ and $\Omega^{E-I} = 0$ on $\mathcal{S}_k^s \setminus (\mathcal{S}_k^s \cap \mathcal{S}_k^{E-I})$. We observe that $0 \leq \mathcal{E}_w(\tau_k) \leq 2$, the lower bound occurs when $\Omega^s \equiv \Omega^{E-I}$ and $\mathcal{S}_k^s \equiv \mathcal{S}_k^{E-I}$, while the upper bound occurs if we assume that both schemes preserve volume and that $\mathcal{S}_k^s \cap \mathcal{S}_k^{E-I} = \emptyset$. The quantity $\mathcal{E}_F(\tau_k)$ represents the *relative footprint error* measured by the ratio of the areas of the two regions \mathcal{S}_k^s and \mathcal{S}_k^{E-I} that lie outside their intersection $\mathcal{S}_k^s \cap \mathcal{S}_k^{E-I}$ divided by the area occupied by the synthetic fracture. We note that $0 \leq \mathcal{E}_F(\tau_k)$, where the lower bound corresponds to $\mathcal{S}_k^s = \mathcal{S}_k^{E-I}$. There is not necessarily an upper bound on $\mathcal{E}_F(\tau_k)$ because there is no reason for the areas to be preserved or even to be finite. If $\mathcal{S}_k^s \cap \mathcal{S}_k^{E-I} = \emptyset$, then $\mathcal{E}_F(\tau_k) \geq 1$.

4.1.3. Observation tiltmeter array and measurement noise. We use a planar array of tiltmeters located at a grid of nodal coordinates defined as follows:

$$\chi = \{a : h : b\}, \eta = \{a : h : b\}, \zeta = d. \quad (4.2)$$

We assume that tilt components with respect to the ζ -axis are measured at each tiltmeter station on this grid, so that a time-series comprising the following components of the rotation vector: $\omega_\chi = u_{\zeta,\eta} - u_{\eta,\zeta}$ and $\omega_\eta = u_{\chi,\zeta} - u_{\zeta,\chi}$, are generated by the synthetic model. We will model noise and measurement errors by adding to each tilt measurement $\omega(\chi_j, \eta_j, \zeta_j, \tau_k)$ white noise that is normally distributed, having a mean of zero and a variance of 1, i.e. $N(0, 1)$, and which has an amplitude of $\sigma_N \omega_{\max,j}$ and is independent of all the other noise components. Thus the measurements that are fed to the EKF-ILSA scheme are as follows:

$$\omega(\chi_j, \eta_j, \zeta_j, \tau; \sigma_N) = \omega(\chi_j, \eta_j, \zeta_j, \tau) + \sigma_N \times \omega_{\max,j} \times N(0, 1). \quad (4.3)$$

For the amplitude components, we assume that $\omega_{\max,j} = \max_k \{\omega(\chi_j, \eta_j, \zeta_j, \tau_k)\}$ and that $\sigma_N \times 100$ is a parameter that represents the percentage noise introduced into the measurements.

4.1.4. Near-field and far-field regimes. Lecampion *et al* [16] have identified a criterion to distinguish far-field from near-field regimes for tiltmeter measurements. By means of far-field asymptotic expansions of the displacement gradients, this criterion was derived based on the ability to distinguish a geometric change represented by the difference between the tilt field of a square DD of side length $2c$ and that due to a point DD of equivalent volume using tilts in a plane a distance d away. The criterion is as follows: if the dimensionless distance $\delta = \frac{d}{2c} < 1.5 = \delta_c$, then the tilt measurements are considered to be near-field, while if $\delta > \delta_c$ the tilt measurements are considered to be far-field. In the experiments, we will vary d in order to be able to test the EKF-ILSA scheme both in the near-field and the far-field regimes. To use this criterion, we take the critical dimension to be the side length $2c = \sqrt{\mathcal{A}[\mathcal{S}]}$ of a hypothetical square having an equivalent area to that of \mathcal{S} . Here operator $\mathcal{A}[\cdot]$ is the same as that defined in (4.1). For a fixed d , this ratio will decrease as the fracture enlarges, so a fracture can move from one regime to another as it evolves.

4.2. Monitoring an HF in a medium with a stress gradient

In the first experiment, the synthetic tiltmeter data were generated by considering an HF propagating in the viscous regime in a linearly varying *in situ* confining stress field. The

confining stress field $\Sigma_o\varphi(\chi, \eta)$, which was introduced in (2.2), is assumed to have the following form:

$$\varphi(\chi, \eta) = \frac{\eta_M - \eta}{\eta_M - \eta_m},$$

where $\eta_m = 0.25$ and $\eta_M = 32.25$ are the minimum and maximum η coordinates of the rectangular mesh. In all the experiments considered in this subsection, we use a mesh size $\Delta\chi = \Delta\eta = 0.5$ and a time-step $\Delta t = 3.18$. As a starter solution we considered the solution of a small penny-shaped fracture propagating in the viscosity dominated regime [30, 24], which has an initial radius $\rho = 2.25$ at a time $\tau = 13.94$. This problem represents a buoyancy-driven hydraulic fracture (see for example [28, 37]) as can easily be seen by re-writing the fluid-flow equation (2.3) in terms of the net pressure $\Pi = \Pi_f - \Sigma_o\varphi(\chi, \eta)$. Eliminating Π_f in favor of Π , we obtain the following additional term:

$$\frac{\Sigma_o}{\mathcal{G}_m} \nabla \cdot (\Omega^3 \nabla \varphi(\chi, \eta)) = - \frac{\Sigma_o}{\mathcal{G}_m(\eta_M - \eta_m)} \frac{\partial \Omega^3}{\partial \eta} \quad (4.4)$$

on the right-hand side of (2.3). This first-order, convective, buoyancy term represents the tendency of the fracture to follow the line of least resistance, which is to grow preferentially in the vertical η direction. For the forward model used with the EKF-ILSA scheme, we assume no confining stress field so that $\varphi(\chi, \eta) \equiv 0$ so the EKF-ILSA scheme has no knowledge of the buoyancy term. This is considered to be a rigorous test of the EKF-ILSA scheme as it introduces significant unmodeled dynamics into the equations governing the evolving synthetic hydraulic fracture that are not seen by the EKF-ILSA scheme except via the feedback from the tiltmeter measurements.

4.2.1. Near-field monitoring without noise. We select the following values for the tilt array parameters that are defined in (4.2): $a = 0$, $b = 32$, $h = 9$ and $d = 10$. For the range of front positions shown in figure 2, the dimensionless distance parameter δ falls in the interval $2.51 \geq \delta \geq 0.57$, which implies that the fracture transitions regimes as it grows and passes the critical value $\delta_c = 1.5$. Indeed, for a brief initial period $13.94 \leq \tau \lesssim 45$ the evolving fracture operates in the far-field regime for this tiltmeter array, after which it spends the majority of the time in the near-field regime.

In figure 2 we plot the synthetic and EKF-ILSA fracture fronts and the corresponding fracture widths at the time-steps $\tau_{25} = 94.97$, $\tau_{50} = 174.53$, $\tau_{75} = 254.09$, and $\tau_{100} = 333.65$ for different values of ϕ . Consistent with the discussion about the characteristics of the EKF for different values of γ (see the discussion that follows (3.10)), we observe that the best identification of the front positions and widths are achieved for the choice $\phi = \sqrt{\gamma} = 0.1$, and that these estimates degrade as ϕ is increased. For small values of ϕ , the EKF places relatively more weight on the measurements than on the dynamics of the forward model. The slight asymmetry in the estimated front positions is due to the fact that the tilt array is not completely symmetrically positioned relative to the axes of symmetry of the synthetic fracture. We observe that as the time period over which the EKF-ILSA estimation scheme has been operating increases, the front and width estimates improve due to the improved estimates of the covariance matrices $\Gamma_{k+1|k+1}$ accumulated over the duration of the HF process.

To see how the estimates of $\partial\mathcal{S}$ and Ω evolve with time, we plot the error measures \mathcal{E}_F and \mathcal{E}_w in figure 3. In these plots the times, $\tau_k : k = 25 : 25 : 100$, at which the fronts and widths in figure 2 are sampled, are represented by the solid circles along the τ -axis. We observe that both these errors reduce monotonically as the value of the resolution parameter is decreased, i.e. $\gamma = \phi^2 \rightarrow 0$. Conversely, the solid curves without symbols in each of these figures (shown in red) represent the upper bound errors between the synthetic fracture solution

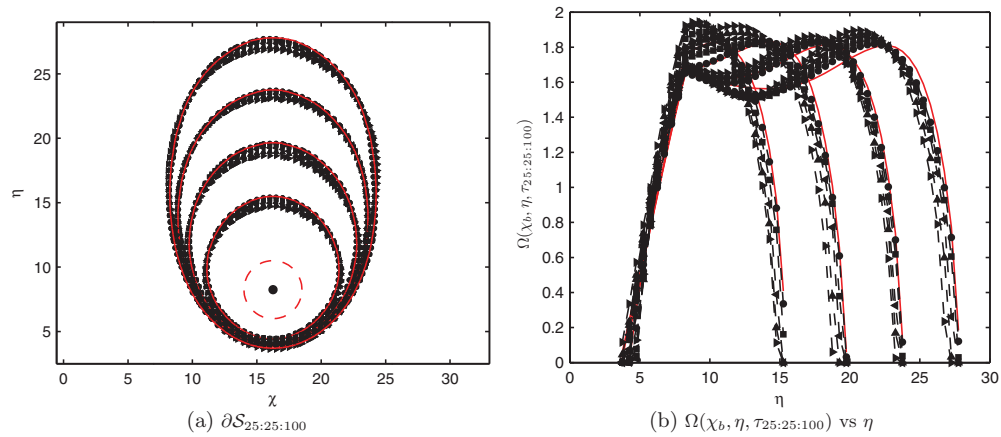


Figure 2. Left figure: the synthetic fronts $\partial S_{25:25:100}$ indicated by the solid line (red) and the corresponding EKF-ILSA front estimates using $\phi = 0.1$ (\bullet), $\phi = 0.5$ (\blacksquare), $\phi = 1.0$ (\blacktriangleleft), $\phi = 1.5$ (\blacktriangle), and $\phi = 2.0$ (\blacktriangleright). The starter fracture is represented by the dashed circle (shown in red). Right figure: vertical cross-sections of the corresponding synthetic width profile and EKF-ILSA estimates $\Omega(\chi_b, \eta, \tau_{25:25:100})$ through the well-bore located at $(\chi_b, \eta_b) = (16.25, 8.25)$. The same symbols have been used as those in part (a) to represent the different ϕ values.

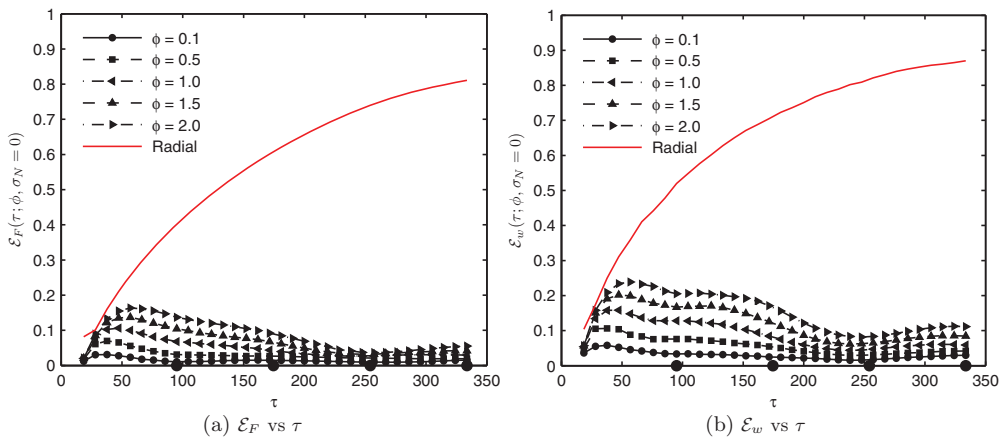


Figure 3. Left figure: time evolution of the footprint error measure \mathcal{E}_F for different values of ϕ . Right figure: time evolution of the width error measure \mathcal{E}_w for different values of ϕ .

with the stress gradient and the radially symmetric viscous solution for which $\gamma = \phi^2 \rightarrow \infty$, in which case the EKF assigns a zero weight to the tilt measurements and only updates for the state dynamics. This latter solution is identical to the radially symmetric solution that would develop in the absence of a stress gradient, i.e. when $\phi(\chi, \eta) = 0$. These plots give a clear measure of the performance of the EKF-ILSA scheme. As time evolves, the errors typically peak relatively early and then ultimately asymptote closer to the end of the identification. We note that the peaks in the errors occur close to the far-field to near-field transition $\tau \approx 45$ so that the subsequent reduction in errors may be due to the fractures moving further into

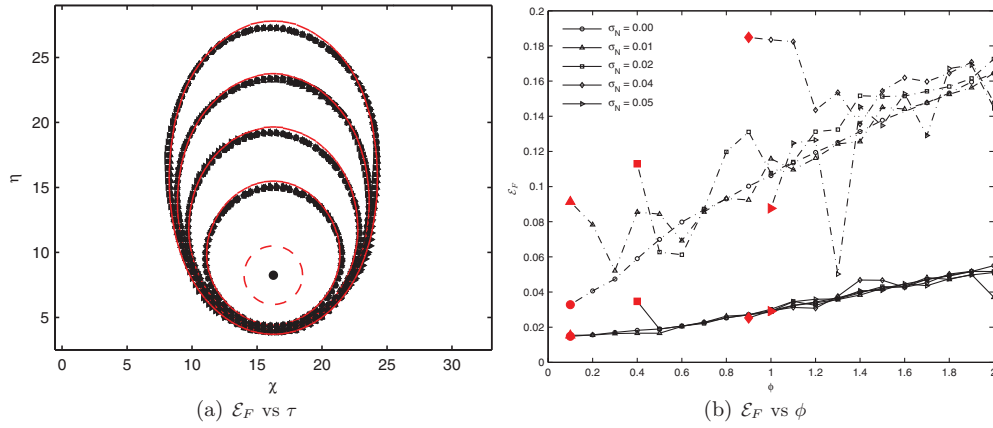


Figure 4. Left figure: the solid lines (red) represent the synthetic fronts while the symbols represent the EKF-ILSA fracture fronts with $\phi = 1.2$, near-field tilts ($d = 10$) and measurements with noise levels $\sigma_N = \{0 (\bullet); 0.01 (\blacksquare); 0.02 (\blacktriangleleft); 0.04 (\blacktriangle); 0.05 (\blacktriangleright)\}$. Right figure: variation of the footprint error measure maxima $\mathcal{E}_{\max,F}$ (-.-) and asymptotes $\mathcal{E}_F(\tau_{100})$ (solid lines) versus ϕ for different values of σ_N .

the near-field regime as they enlarge. These reductions in error as time evolves could also, in part, be due to the improved estimates of the covariance matrix $\Gamma_{k+1|k+1}$ accumulated as time advances.

4.2.2. Near-field monitoring including noise. We repeat the estimation process with the same tilt array and parameters as described in the previous subsection 4.2.1, but this time we include the noise defined in (4.3) in which $\sigma_N > 0$. In figure 4(a), we use the same sample times as above to compare the synthetic and the EKF-ILSA fracture fronts assuming that $\phi = 1.2$ and that $\sigma_N \geq 0$. We observe that there is very little spread due to the increased noise in the measurements, while the fracture fronts are still identified relatively accurately. This situation is not true for all choices of $0 < \phi \leq 2$. If ϕ is too small, then the EKF-ILSA scheme places too much weight on the measurements, which, if subjected to significant noise, can introduce undesirable perturbations to the estimated fracture footprints to the point that the scheme becomes unstable. This figure demonstrates that increasing ϕ can significantly improve robustness while compromising little on resolution. To illustrate the performance characteristics of the EKF-ILSA scheme in the ϕ - σ_N space, in figure 4(b) we plot the error maxima $\mathcal{E}_{\max,F}$ (-.- lines) and asymptotes $\mathcal{E}_F(\tau_{100})$ (solid lines) as a function of ϕ for a number of different values of the noise parameter σ_N . These maxima and asymptotes are evident in figure 3(a). A number of interesting characteristics of the EKF-ILSA scheme become evident from this figure. (i) The asymptotic error $\mathcal{E}_F(\tau_{100})$ exhibits roughly a linear increase with ϕ that is largely independent of the noise level σ_N . The error maxima $\mathcal{E}_{\max,F}$ exhibit a similar linear increase with ϕ , but the fluctuations about this straight line are more marked. (ii) As the noise level σ_N increases, so too does the minimal ϕ value required to stabilize the EKF-ILSA scheme need to increase. To represent this in figure 4(b), we have, for each σ_N , colored (red) and enlarged the symbol representing the smallest ϕ value for which the EKF-ILSA scheme is still stable. Finally, combining these two characteristics, we see that a compromise in resolution is required in order to increase the robustness needed to deal with additional noise.

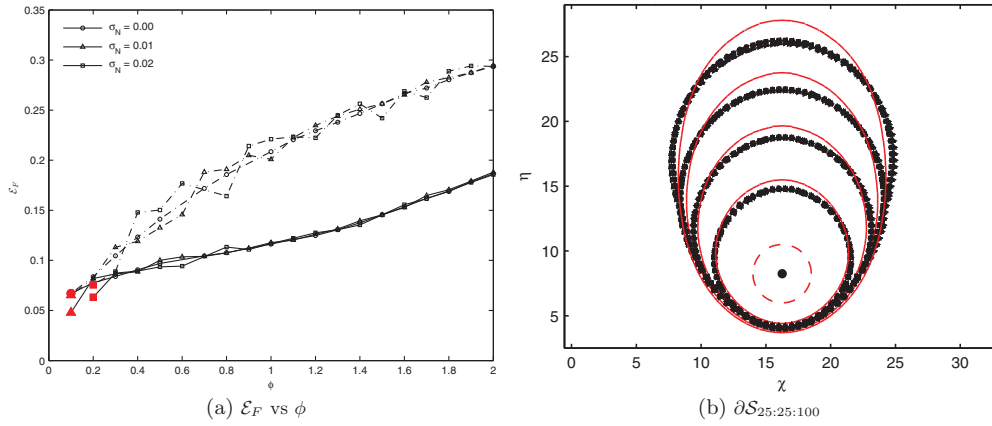


Figure 5. Left figure: variation of the footprint error measure maxima $\mathcal{E}_{\max,F}$ (---) and asymptotes $\mathcal{E}_F(\tau_{100})$ (solid lines) versus ϕ for different values of σ_N . A 4×4 tilt array with $h = 9$ was used for all these experiments. Right figure: synthetic footprints represented by the solid lines (shown in red) and the $\phi = 0.6$ far-field tilt EKF-ILSA fracture fronts represented by the following symbols corresponding to the measurements noise levels $\sigma_N = \{0$ (\bullet); 0.01 (\blacksquare); 0.02 (\blacktriangleleft); 0.03 (\blacktriangleright)}. A more dense 5×5 tiltmeter array with $h = 7$ is used.

4.2.3. Far-field monitoring including noise. For the results presented in this subsection, we select the following values for the tilt array parameters defined in (4.2): $a = 0$, $b = 32$, $h = 7$ and 9 , and $d = 50$. For this case, the dimensionless distance parameter δ falls in the interval $\delta_c < 2.85 \leq \delta \leq 11.51$, which implies that the fracture remains in the far-field regime throughout its evolution. In figure 5(a), we use the same format as that used above to summarize the results for this series of numerical experiments. The values of the footprint error measure maxima $\mathcal{E}_{\max,F}$ and asymptotes $\mathcal{E}_F(\tau_{100})$ are plotted as a function of ϕ . In this figure, we use the same 4×4 tilt array with $h = 9$ as that used above. As with the near-field case, these parameters increase almost linearly with increasing ϕ . However, the error level is notably larger for the far-field case $d = 50$ than for the near-field case $d = 10$. For example, the asymptotic error $\mathcal{E}_F(\tau_{100})$ for the near-field case ($d = 10$) lies in the range 1.48–5.50 % (with a gradient of 0.021) compared to a range of 6.70–18.65 % (with a gradient of 0.059) for the far-field case $d = 50$. It can be seen that it is possible to obtain stable EKF-ILSA identifications for all ϕ in the range $0.1 \leq \phi \leq 2.0$, provided the amplitude of measurement noise is restricted to the range $0 \leq \sigma_N \leq 0.02$. In order to achieve a stable identification for larger noise amplitudes $\sigma_N > 0.02$, it is necessary to use larger values of the resolution parameter $\phi \geq 1.3$. The footprint error measure in this case will range between 13.13 % and 24.4 %, or larger. Thus for a far-field tilt array one is presented with a difficult choice. In order to achieve an identification of the fracture footprint within 10%, it is necessary to use a resolution parameter in the range $0 < \phi \leq 0.6$, but then the EKF-ILSA scheme becomes more susceptible to noise resulting in significant perturbations in the identified front and instabilities in the algorithm. Indeed, using the 4×4 tilt array with $h = 9$ on the far-field measurements $d = 50$, these perturbations and instabilities are observed for $\sigma_N > 0.02$ when ϕ is in the range $0 < \phi \leq 1.3$.

However, it is possible to make the tilt array significantly more robust by increasing the density of tiltmeters in a given region. Although we expect that increasing the density of tilts can degrade the overall conditioning of the system, due to redundancy in the measurements, it is this redundancy in measurements that enables the EKF-ILSA algorithm to distinguish noise

from measurement by essentially canceling the random fluctuations—provided the noise in the different tilt locations is independent. In figure 5(b), we plot the EKF-ILSA identifications of the front locations for $\phi = 0.6$, measurement noise amplitudes $0 \leq \sigma_N \leq 0.04$ and using a 5×5 tiltmeter array with $h = 7$. While the performance of the EKF-ILSA scheme is clearly worse for this far-field case than it is for the near-field case, the identifications are still fairly accurate and show significant robustness to perturbations introduced by noise in the measurements.

4.3. Monitoring an HF in a medium with a symmetric stress jump

The numerical experiments considered in this subsection are motivated by the symmetric stress jump experiments reported in [11], in which an HF is initiated within a channel having a low confining stress, which is sandwiched between two regions in which there is a high confining stress. The extent to which the HF penetrates the high stress zones is of great practical interest in the oil industry. To simulate data from this type of situation, we generate synthetic tiltmeter data by considering a viscosity-driven HF propagating in an elastic medium in which the well bore is located midway between two jump discontinuities in the confining stress field $\Sigma_o \varphi(\chi, \eta)$. In particular, the well bore is located at $(\chi_b, \eta_b) = (7.1667, 7.1667)$, while the confining stress has the following jump discontinuities across the planes $\eta = 6.6667$ and $\eta = 7.6667$:

$$\Sigma_o = 3/4; \quad \varphi(\chi, \eta) = \begin{cases} 1 & \text{if } |\eta - \eta_b| \geq 1/2 \\ 0 & \text{if } |\eta - \eta_b| < 1/2. \end{cases} \quad (4.5)$$

To generate the synthetic tilt measurements, we use a rectangular mesh comprising square elements whose edges are defined by the Cartesian product of the following partitions $\chi_k = 0 : \Delta\chi : 14.3333$ and $\eta_k = 0 : \Delta\eta : 14.3333$, where $\Delta\chi = \Delta\eta = 1/9$. A radially symmetric starter crack is assumed in which the initial radius is set to $\rho = 0.2778$ at time $\tau_1 = 0.1260$ and the pressure and width profiles are initialized to the radially symmetric viscous solution [30]. The time duration of the simulation is assumed to be $\tau_1 \leq \tau \leq 21.5521$, which is subdivided into 300 uniform time-steps of size $\Delta\tau = 0.0713$. The EKF-ILSA scheme assumes a forward model for which $\varphi(\chi, \eta) = 0$, so that a radially symmetric fracture would develop without an update from the measurements via the EKF component of the algorithm.

The tilt array in this case is defined by the parameters $a = 0$, $b = 16$, $h = 3$ and 1, and $d = 10$. The effective square side length, having an area equivalent to the evolving fracture footprint, is initially $2c = 0.49235$ and is increased to $2c = 4.5165$ by the end of the simulation. This corresponds to a dimensionless distance parameter δ in the range $20.3108 \geq \delta \geq 2.2141 > \delta_c$ so the fracture remains in the far-field regime throughout.

In figure 6(a), we plot the evolving synthetic fracture fronts for $\tau_k : k \in \{10, 20, 30, 50, 75, 100 : 50 : 300\}$ and the corresponding fracture fronts identified by the EKF-ILSA scheme with $\phi = 0.01$ and no noise, $\sigma_N = 0$. We have chosen a particularly small value of the resolution parameter to demonstrate that the EKF-ILSA scheme can compensate for significant unmodeled dynamics and resolve these extreme changes in fracture geometry by taking into account the tilt measurements. For this run, a 6×6 tiltmeter array with spacing $h = 3$ is used. Unfortunately, the EKF-ILSA scheme is not robust to noise in the measurements for such a small value of ϕ . In the previous subsection, we found that robustness to noise could be traded for resolution by increasing the parameter ϕ . However, for this problem, with extreme changes in the geometry, even a moderate increase in the resolution parameter ϕ results in a significant degradation in the quality of the identified fracture footprints. This is illustrated in figure 6(b) in which we plot the same sequence of fracture fronts corresponding to $\phi = 0.4$. It is clear that if we want to achieve a reasonably accurate EKF-ILSA identification of the

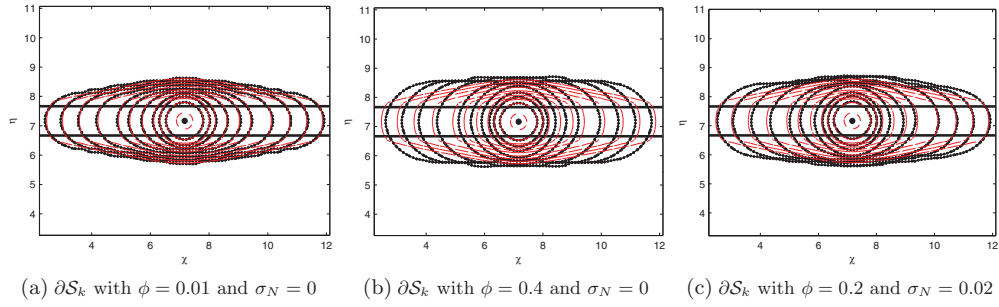


Figure 6. These figures show a sub-sequence of the fracture fronts ∂S_k for selected pairs (ϕ, σ_N) in which the synthetic solution is represented by solid line segments (in red) and the EKF-ILSA solution by solid lines with the \bullet symbols.

fracture footprints for this problem, we will have to use a relatively small value of the resolution parameter, $\phi = 0.2$ for example. In order to achieve robustness to noise for such a small value of ϕ it will be necessary to make use of a tilt array with a greater density to exploit the noise cancelation effect achieved by the additional redundancy in measurements. To this end we reduce the array spacing parameter from $h = 3$ to $h = 1$. In figure 6(c), we plot results for the EKF-ILSA identification of the symmetric stress jump footprints using the more dense tiltmeter array $h = 1$, $\phi = 0.2$ and assuming a noise amplitude $\sigma_N = 0.02$. These front identifications are clearly an improvement on those shown in part (b) of this figure despite the noise in the measurements.

4.4. Monitoring an HF in a medium with an asymmetric stress jump

The numerical experiments considered in this subsection are motivated by the asymmetric stress jump experiments reported in [42], in which an HF is initiated within a channel, having an intermediate confining stress, which is sandwiched between a high-stress region and a low-stress region. We consider precisely the same configuration of layers as in the previous subsection except that the confining stress field has the following form:

$$\Sigma_o = 1; \varphi(\chi, \eta) = \begin{cases} 1 & \text{if } \eta - \eta_b \geq 1/2 \\ 1/2 & \text{if } |\eta - \eta_b| < 1/2 \\ 0 & \text{if } \eta - \eta_b \leq -1/2. \end{cases} \quad (4.6)$$

In this case, the fracture penetrates very little into the higher stress region, propagates only a moderate distance in the intermediate stress region and herniates dramatically into the low-stress region in which the majority of the fracture footprint and fluid volume ultimately reside. To generate the synthetic tilt measurements, we use the same run parameters, mesh, starter fracture and time-step as that used for the symmetric stress jump described in subsection 4.3. As before the EKF-ILSA scheme assumes a forward model for which $\varphi(\chi, \eta) = 0$ and would generate a radially symmetric fracture without input from the tilt measurements. The tilt array in this case is defined by the parameters $a = 0$, $b = 16$, $h = 1$ and 3, and $d = 50$. The effective square side-length, having an area equivalent to the evolving fracture footprint, is initially $2c = 0.49235$ and is increased to $2c = 4.8403$ by the end of the simulation, which corresponds to a dimensionless distance parameter $101.5538 \geq \delta \geq 10.3299 > \delta_c$ in the far-field regime throughout.

In figure 7(a) we compare the synthetic fracture fronts with those obtained by EKF-ILSA identification assuming $\phi = 0.1$ and no noise. The EKF-ILSA scheme provides a very good

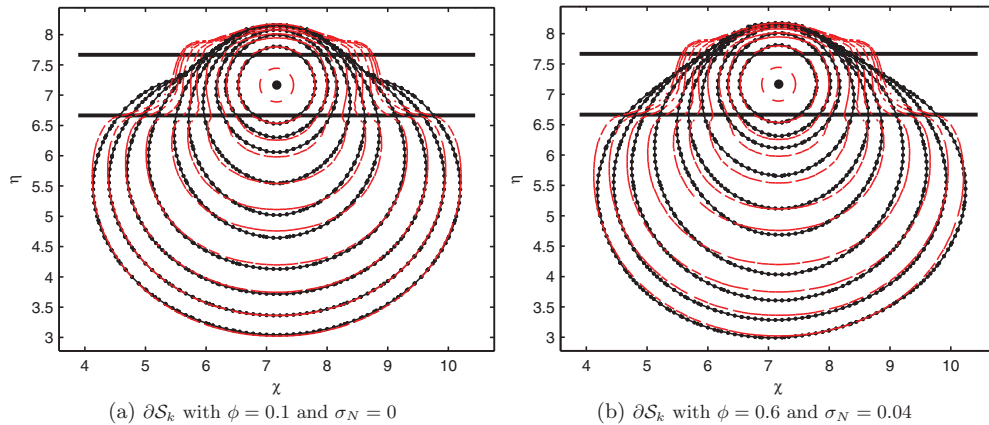


Figure 7. Using the same symbol convention as in figure 6 we plot the EKF-ILSA solution with and without noise.

identification of the fracture front positions in the low-stress region where the fracture has herniated and the widths are large. However, in the high-stress region, where the fracture opening is relatively small, the EKF-ILSA is not able to identify all the details of the fracture footprints as the fracture widths are much smaller than in other parts of the fracture. The relatively poor match of the fracture footprint in the high-stress region affects the way in which the footprint is approximated in the intermediate stress zone between the stress jump interfaces. The EKF-ILSA fronts show a moderate inflection point in this region and are only able to approximate the synthetic fracture fronts in an average sense.

It is interesting to contrast the performance of the EKF-ILSA scheme for this asymmetric fracture with that of the symmetric fracture discussed in subsection 4.3. Though both tilt arrays in these two examples are operating in the far-field regime, the array for the asymmetric stress jump is five times farther from the fracture than in the case of the symmetric stress jump. In spite of this, the tilt array in the asymmetric case is able to capture the fracture footprint much more accurately than in the symmetric case. This discrepancy can be explained by observing that, in the symmetric case, the majority of the front identification takes place in the high-stress regions where the fracture widths are relatively small compared to the widths in the well-bore channel. Indeed, the identification of the fracture fronts in the channel region is particularly accurate. In contrast, for the asymmetric case, the majority of the fracture front is being identified in the herniated region where the fracture widths are much larger than in the remainder of the fracture. In figure 7(b), we compare the fracture footprints for the synthetic and EKF-ILSA identification assuming $\phi = 0.6$ and a noise level $\sigma_N = 0.04$. To achieve robustness for such a large noise amplitude, it is necessary to decrease the sample spacing of the tilt array to $h = 1$. Compared to the plots shown in part (a), we observe some degradation in the identification of the front positions with the increase of ϕ , but this identification is still remarkably accurate given the level of noise. The slight asymmetry in the results is due to the fact that the tilt array is not distributed symmetrically with respect to the well bore in the χ -direction.

5. Conclusions

In this paper, we propose a novel algorithm to invert time-series of tiltmeter measurements sampled at selected points within an elastic medium in order to identify the fracture footprints

and fracture opening as an HF propagates. The algorithm is based on integrating the EKF with the stable and efficient ILSA, recently developed to solve the highly nonlinear degenerate integro-partial differential equations governing the dynamics of the moving fracture front. The unique property of the ILSA scheme is that it uses predicted state values close to fracture tip along with the tip asymptotic relation, for a given propagation regime, to locate the fracture-free boundary. This feature enables integration with the EKF without having to resort to explicit parametrization and identification of the fracture-free boundary. The proposed scheme uses the EKF state predictions and measurement updates, assuming a given fracture footprint, to determine corresponding ILSA front updates to arrive at an iterative algorithm that has both state and front updates that are consistent with the measurements.

By means of the appropriate scaling we are able to identify the parameter choices for the EKF component of the algorithm that are suitable for the identification of remote measurements. In particular, we identified the parameter $\gamma = \phi^2$, which determines the relative weight the Kalman filter places on the observed measurements compared to the state predicted by the dynamic model. This interpretation of the parameter choices is corroborated in all the numerical experiments.

We considered three numerical experiments comprising different physical situations each of which has real-world realizations: buoyancy-driven fracture propagation, breakthrough by an HF propagating in a channel formed by a symmetric stress jump and an asymmetric stress jump. Some interesting patterns emerge from the numerous numerical results presented. (i) The EKF-ILSA scheme provides successful identifications in both the near-field and far-field regimes. As is to be expected, the resolution is better in the near-field regime than in the far-field regime. (ii) The EKF-ILSA scheme footprint and width errors initially increase to a maximum level after which they decrease and eventually tend to an asymptote. This characteristic can be explained by the improved estimates of the state covariance matrix $\Gamma_{k|k}$ as the data are accumulated. (iii) The resolution of the identification degrades roughly linearly with increasing ϕ —as more weight is taken away from the measurements and placed on the state evolution model. (iv) The EKF-ILSA scheme can tolerate noise of up to 5% of the maximum measurement amplitude. The robustness to noise in the measurements typically increases as ϕ is increased. Another way in which an array of tiltmeters can be made more robust to noise in the measurements is to increase the density of tilts in a given region. In this way, the EKF-ILSA scheme can exploit the redundancy in the additional measurements by canceling the independent fluctuations in measurements from neighboring stations. Increasing the density of tilts typically does not improve the error characteristic but does improve the robustness. Though the deployment of extremely dense arrays to improve robustness to noise may not be practical at this time, this noise cancellation feature of the EKF-ILSA scheme might be an important consideration in deciding the placement of tiltmeters or to provide a stimulus for the development of new tiltmeter technology.

Having established the basic methodology a number of developments and extensions of the EKF-ILSA scheme can be considered. The EKF is based on a linearization of the state equation (3.1) about a nominal state comprising the estimate at the previous update. However, there is a limit to the validity of this form of linear approximation especially in the light of the fact that the EKF update equations are derived by taking conditional expectations of the linearized system. However, for an arbitrary nonlinear function $f(x)$ and random variable x it is, in general, definitely not true that $E[f(x)|y] = f(E[x|y])$, which is a fundamental approximation made in the linearization procedure used to formulate the EKF. This error is compounded even further in the calculation of the covariance matrices. Different approaches to evaluating these expectations have been developed such as the so-called unscented Kalman filter (UKF) [13, 14, 39]. The UKF approximates the desired expectations by taking appropriate

weighted sums evaluated at so-called sigma points and has been shown to be much more stable than the EKF in the context of highly nonlinear systems. The UKF is typically computationally equivalent to, or even more efficient than, the EKF; however, for the HF problem each new sample point will involve a completely new solution of the system of coupled equations (2.12). Thus the UKF will clearly require more development in this context, which is beyond the scope of this paper.

We believe that this novel EKF-ILSA scheme brings a new approach to the classic elastostatic inverse problem. Having established the potential of the method *in silico* via numerical experiments with synthetic measurements, our next objective is to test the procedure on real-field data. If this is shown to be promising, then there will be a great deal of potential for the development of more efficient algorithms to make the real-time monitoring and possibly even control of propagating hydraulic fractures a reality.

References

- [1] Anderson B D O and Moore J B 1979 *Optimal Filtering* (New York: Dover)
- [2] Bolzon G, Fedele R and Maier G 2002 Identification of cohesive crack models by Kalman filter *Comput. Methods Appl. Mech. Eng.* **191** 2847–71
- [3] Crouch S L and Starfield A M 1990 *Boundary Element Methods in Solid Mechanics* (London: Unwin Hyman)
- [4] Desroches J, Detournay E, Lenoach B, Papanastasiou P, Pearson J R A, Thiercelin M and Cheng A H D 1994 The crack tip region in hydraulic fracturing *Proc. R. Soc. A* **447** 39–48
- [5] Economides M J and Nolte K G (ed) 2000 *Reservoir Stimulation* (New York: Wiley)
- [6] Evans K 1983 On the development of shallow hydraulic fractures as viewed through the surface deformation field: part 1. Principles *J. Pet. Technol.* **35** 406–10
- [7] Garagash D I and Detournay E 2000 The tip region of a fluid-driven fracture in an elastic medium *ASME J. Appl. Mech.* **67** 183–92
- [8] Garagash D I and Detournay E 2005 Plane-strain propagation of a fluid-driven fracture: small toughness solution *ASME J. Appl. Mech.* **72** 916–28
- [9] Hills D A, Kelly P A, Dai D N and Korsunsky A M 1996 *Solution of Crack Problems, The Distributed Dislocation Technique, Solid Mechanics and Its Applications* vol 44 (Dordrecht: Kluwer)
- [10] Ijaz U Z, Khambampati A K, Lee J S, Kim S and Kim K Y 2008 Nonstationary phase boundary estimation in electrical impedance tomography using unscented Kalman filter *J. Comput. Phys.* **227** 7089–112
- [11] Jeffrey R G and Bungler A P 2009 A detailed comparison of experimental and numerical data on hydraulic fracture height growth through stress contrasts *Soc. Pet. Eng. J.* **14** 413–22
- [12] Jeffrey R G and Mills K W 2000 Hydraulic fracturing applied to inducing longwall coal mine goaf falls *Proc. 4th North American Rock Mechanics Symp. (Seattle, Washington, DC, 31 July–3 Aug.)* (Rotterdam: Balkema) pp 423–30
- [13] Julier S, Uhlmann J and Durrant-Whyte H 1995 A new approach for filtering nonlinear systems *Proc. of the American Control Conf.* pp 1628–32
- [14] Julier S J 2002 The scaled unscented transformation *Proc. of the American Control Conf.* vol 6 pp 4555–9
- [15] Kaipio J and Somersalo E 2005 *Statistical and Computational Inverse Problems (Applied Mathematical Sciences* vol 160) (Berlin: Springer)
- [16] Lecampion B, Jeffrey R and Detournay E 2005 Resolving the geometry of hydraulic fractures from tilt measurements *Pure Appl. Geophys.* **162** 2433–52
- [17] Lecampion B and Peirce A 2007 Multipole moment decomposition for imaging hydraulic fractures from remote elastostatic data *Inverse Problems* **23** 1641–58
- [18] Mandel J, Bennethum L S, Beezley J D, Coen J L, Douglas C C, Kim M and Vodacek A 2008 A wildland fire model with data assimilation *Math. Comput. Simul.* **79** 584–606
- [19] Maier G, Bocciarelli M, Bolzon G and Fedele R 2006 Inverse analyses in fracture mechanics *Int. J. Fract.* **138** 47–73
- [20] Mitchell S L, Kuske R and Peirce A P 2007 An asymptotic framework for the analysis of hydraulic fractures: the impermeable case *ASME J. Appl. Mech.* **74** 365–72
- [21] Ojima Y and Kawahara M 2009 Estimation of river current using reduced Kalman filter finite element method *Comput. Methods Appl. Mech. Eng.* **198** 904–11

- [22] Osher S and Fedkiw R 2002 *Level Set Methods and Dynamic Implicit surfaces (Applied Mathematical Sciences vol 153)* (New York: Springer)
- [23] Peirce A 2006 Localized Jacobian ILU preconditioners for hydraulic fractures *Int. J. Numer. Methods Eng.* **65** 1935–46
- [24] Peirce A and Detournay E 2008 An implicit level set method for modeling hydraulically driven fractures *Comput. Methods Appl. Mech.* **197** 2858–85
- [25] Peirce A P and Siebrits E 2005 A dual mesh multigrid preconditioner for the efficient solution of hydraulically driven fracture problems *Int. J. Numer. Methods Eng.* **63** 1797–823
- [26] <http://www.pinntech.com>
- [27] Rice J R 1968 Mathematical analysis in the mechanics of fracture *Fracture: An Advanced Treatise* ed H Liebowitz (New York: Academic) chapter 3, pp 191–311
- [28] Roper S M and Lister J R 2007 Buoyancy-driven crack propagation: the limit of large fracture toughness *J. Fluid Mech.* **580** 359–80
- [29] Rochinha F and Peirce A 2010 Monitoring hydraulic fractures: state estimation using an extended Kalman filter *Inverse Problems* **26** 025009
- [30] Savitski A A and Detournay E 2002 Propagation of a fluid-driven penny-shaped fracture in an impermeable rock: asymptotic solutions *Int. J. Solids Struct.* **39** 6311–37
- [31] Seppanen A, Vauhkonen M, Vauhkonen P J, Voutilainen A and Kaipio J P 2007 State estimation in process tomography—three-dimensional impedance imaging of moving fluids *Int. J. Numer. Methods Eng.* **73** 2141–57
- [32] Salamon M D 1963 Elastic analysis of displacements and stresses induced by the mining of seam or reef deposits: part I *J. South Afr. Inst. Min. Metall.* **64** 128–49
- [33] Sethian J A 1999 *Level Set Methods and Fast Marching Methods: Evolving Interfaces in Computational Geometry Fluid Mechanics Computer Vision and Materials Science* (Cambridge: Cambridge University Press)
- [34] Spence D and Sharp P 1985 Self-similar solutions for elastohydrodynamic cavity flow *Proc. R. Soc. A* **400** 289
- [35] Siebrits E and Peirce A P 2002 An efficient multi-layer planar 3D fracture growth algorithm using a fixed mesh approach *Int. J. Numer. Methods Eng.* **53** 691–717
- [36] Sun R J 1969 Theoretical size of hydraulically induced horizontal fractures and corresponding surface uplift in an idealized medium *J. Geophys. Res.* **74** 5995–6011
- [37] Touvet T, Balmforth N J, Craster R V and Sutherland B R 2011 Fingering instability in buoyancy-driven fluid-filled cracks *J. Fluid Mech.* **672** 60–77
- [38] van As A and Jeffrey R G 2000 Caving induced by hydraulic fracturing at North Parkes mines *Pacific Rocks 2000* (Rotterdam: Balkema) pp 353–60
- [39] van der Merwe R 2004 Sigma-point Kalman filters for probabilistic inference in dynamic state-space models *PhD Thesis* OGI School of Science & Engineering, Oregon Health & Science University
- [40] Warpinski N R, Griffin L G, Davis E J and Grant T 2006 Improving hydraulic fracture diagnostics by joint inversion of downhole microseismic and tiltmeter data *SPE 102690: SPE Annu. Tech. Conf. and Exhibition (San Antonio, TX, 24–27 Sep.)* pp 10
- [41] Wright C A, Davies E J, Minner J F, Weijers L, Schnell E J and Hunter S P 1998 Surface tiltmeter fracture mapping reaches new depths—10,000 feet and beyond? *SPE 39919: SPE Regional Meeting on Low Permeability Reservoirs Symp. (Denver, CO, 5–8 April)* pp 8
- [42] Wu R, Bungler A P, Jeffrey R G and Siebrits E 2008 A comparison of numerical and experimental results of hydraulic fracture growth into a zone of lower confining stress *ARMA 08-267: Proc. 2nd US–Canada Rock Mechanics Symp. (San Francisco, CA, USA, 29 June–2 July)* p 267
- [43] Xu W, Le Calvez J and Thiercelin M 2009 Characterization of hydraulically-induced fracture network using treatment and microseismic data in a tight-gas formation: a geomechanical approach *SPE Tight Gas Completions Conf. (San Antonio, TX, USA, 15–17 June 2009)*